

Temperature and composition insensitivity of thermoelectric properties of high-entropy half-Heusler compounds

Suwei Li^a, Kan Chen^a, Yichen Wang^a, Theo Saunders^a, Ruizhi Zhang^a, Jan-Willem G. Bos^b, Michael J. Reece^{a,*}

^a School of Engineering and Materials Science, Queen Mary University of London, Mile End Road, London E1 4NS, UK

^b EaStCHEM, School of Chemistry, University of St Andrews, North Haugh, St Andrews, KY16 9ST, UK

ARTICLE INFO

Keywords:

Half-Heusler
High entropy
Thermoelectric
Temperature insensitivity
Composition insensitivity

ABSTRACT

Composition modification by doping and solid solution is a well-studied strategy in thermoelectric (TE) materials to optimize their properties. Recently, the concept of entropy stabilization has offered the possibility of forming random solid solutions that have properties that go beyond the rule of mixture. In this study, we prepared a series of high-entropy half-Heusler solid solutions (HEHHs) with varying valence electron counts (VEC), $(\text{Ti}_{0.33}\text{Zr}_{0.33}\text{Hf}_{0.33})_{1-x}(\text{V}_{0.33}\text{Nb}_{0.33}\text{Ta}_{0.33})_x\text{CoSb}$ ($x = 0.5$ to 0.75). Compared to their medium- and low-entropy counterparts, the TE properties of HEHHs are less sensitive to temperature and composition variation (charge carrier concentration efficiency of $\sim 10\%$). An ultra-low lattice thermal conductivity for half-Heusler of $1.19 \text{ W}\cdot\text{m}^{-1}\cdot\text{K}^{-1}$ was achieved.

1. Introduction

Sustainable energy technology is a critical research area because of the energy crisis and climate change [1]. Thermoelectric (TE) materials can realize direct conversion between heat and electricity without carbon dioxide emission. The performance of a TE material is quantified by a dimensionless figure-of-merit defined as $ZT = \alpha^2 \sigma \kappa^{-1} T$, where α is the Seebeck coefficient, σ is the electrical conductivity, κ is the thermal conductivity, and T is the absolute temperature. The ability to convert energy is related to the power factor ($PF = \alpha^2 \sigma$). κ is the sum of the electronic (κ_E) and the lattice (κ_L) contributions to the thermal conductivity, $\kappa = \kappa_E + \kappa_L$ [2].

Composition modification by doping and solid solution are commonly used methods to improve the TE performance of materials by modifying their charge carrier concentration [3–5]. In some cases, selective dopants can even decouple σ and α due to band degeneracy [6]. To reduce κ , researchers often introduce selected atoms with large mass and size differences into the crystal lattice, which leads to significant lattice distortion and increased phonon scattering [7–9].

Since 2004, high-entropy alloys (HEAs) with equimolar composition have gained considerable attention for their promising effects such as entropy stabilization, sluggish diffusion, lattice distortion, and the cocktail effect [10–12]. In recent years, the high-entropy concept has

been extended to ceramics including oxides [13], carbides [14,15], borides [16], nitrides [17], and chalcogenides [18,19], which have been widely used as structural [15], catalytic [20], electrode [21], capacitor [22], and TE materials [18,23–25]. In contrast to traditional binary or ternary TE materials, high-entropy TE materials possess a complex crystal lattice comprising of multiple cations or anions with long range structural order but chemical disorder. The complexity of the structure and composition can enhance lattice distortion and reduce κ [26–29]. However, our knowledge of the effect of multi-components on their electrical performance is incomplete.

Half-Heusler (HH) compounds, a variant of Heusler compounds, with the elemental formula XYZ located on three face-centered cubic (fcc) sublattices, have attracted significant attention for TE applications due to their high PF [30]. X is a transition metal with low electronegativity (e.g. Ti, Zr, Hf in group IVB and V, Nb, Ta in group VB) occupying Wyckoff positions 4a (0, 0, 0), Y is a transition metal with higher electronegativity (e.g. Fe, Co, and Ni) occupying Wyckoff positions 4c (1/4, 1/4, 1/4), and Z is a main group element (e.g. Sn and Sb) occupying Wyckoff positions 4b (1/2, 1/2, 1/2). The multiple choices of X, Y, and Z elemental species provides the possibility of realizing stable HH compounds using the entropy stabilization concept. Zintl chemistry suggests that the TE performance and phase stability of both XNiSn (n-type) and XCoSB (p-type) are highly related to the 18 valence electron count (VEC)

* Corresponding author.

E-mail address: m.j.reece@qmul.ac.uk (M.J. Reece).

<https://doi.org/10.1016/j.actamat.2024.119761>

Received 6 July 2023; Received in revised form 29 January 2024; Accepted 14 February 2024

Available online 15 February 2024

1359-6454/© 2024 The Authors. Published by Elsevier Ltd on behalf of Acta Materialia Inc. This is an open access article under the CC BY-NC-ND license (<http://creativecommons.org/licenses/by-nc-nd/4.0/>).

rule, and can be further optimized by doping [31]. Due to these unique features, HH compounds are ideal materials for investigating the thermal and electrical transport behavior of multi-component systems.

In this work, equimolar group IVB elements (Ti, Zr, and Hf) and equimolar group VB elements (V, Nb, and Ta) were added on the X site to form a series of high-entropy half-Heusler solid solutions (HEHHs) $(\text{Ti}_{0.33}\text{Zr}_{0.33}\text{Hf}_{0.33})_{1-x}(\text{V}_{0.33}\text{Nb}_{0.33}\text{Ta}_{0.33})_x\text{CoSb}$ ($x = 0.5$ to 0.75). Changing the ratio of the group IVB and VB elements was used to modify the charge carrier concentration, as is typically done in HHs by substitution of, for example, iron on the Y-site [24] or tin on the Z-site. The effect of multi-components was studied by comparing the TE related properties and bonding features of HEHH compounds with medium- or low-entropy counterparts. The HEHH compounds demonstrated stronger polar bonding, temperature insensitivity of electrical properties, low doping/solid solution carrier concentration efficiency, and ultra-low κ_L with temperature insensitivity.

2. Methods

2.1. Sample synthesis

Polycrystalline $(\text{Ti}_{0.33}\text{Zr}_{0.33}\text{Hf}_{0.33})_{1-x}(\text{V}_{0.33}\text{Nb}_{0.33}\text{Ta}_{0.33})_x\text{CoSb}$ ($x = 0.5$ to 0.75) compounds were synthesized by ball milling high-purity Ti (-325 mesh, 99.99 %, Alfa Aesar), Zr (-325 mesh, 99.5 %, Sigma Aldrich), Hf (-325 mesh, 99.99 %, Alfa Aesar), V (-325 mesh, 99.5 %, Alfa Aesar), Nb (-325 mesh, 99.8 %, Alfa Aesar), Ta (-325 mesh, 99.97 %, Alfa Aesar), Co ($-100+325$ mesh, 99.8 %, Alfa Aesar), and Sb (-100 mesh, 99.5 %, Alfa Aesar) in appropriate stoichiometric ratios. The high quality of the powder precursors was validated through EDS point analysis of the precursor powders conducted before ball milling, as illustrated in Fig. S1 (Supporting Information). An investigation of Fe substitution on the Co site for similar high-entropy materials is reported in our previous work [24]. All of the powders (10 gs in total) were loaded into 250 mL stainless steel jars, containing 10 mm diameter stainless steel balls, in an argon-filled glove box (oxygen < 1 ppm). The weight ratio of the powders to balls was 1:20. Ball milling was performed for 10 h at a milling rate of 300 rpm using a PULVERISETTE 5/4 planetary ball mill machine (Fritsch, Germany). The fine powders after ball milling were sintered in a spark plasma sintering (SPS) furnace (FCT HPD 25, FCT System GmbH, Germany) under a uniaxial pressure of 60 MPa at 900 °C for 5 mins to obtain 13 mm diameter bulk samples. The high density (around 95 % of the theoretical density) of the samples was confirmed by the Archimedes method in all bulk samples.

2.2. Sample characterization

The phases of the powders after ball milling and SPS processing (crushed sample) were examined by X-ray diffraction (XRD, PANalytical X'Pert Pro-Instrument using Cu K α radiation). The fracture surface and compositional analysis of sintered pellets were observed using a field-emission scanning electron microscope (SEM, FEI, Inspect F, 20 kV) with an energy-dispersive spectrometer (EDS). X-ray photoelectron spectroscopy (XPS, ThermoFisher Nexsa, ThermoFisher Scientific Inc) was performed for chemical composition and chemical state analysis with an Al K α X-ray source. The spot size, binding energy step, and argon ion etch time for XPS testing were 100 μm , 0.1 eV, and 10 mins, respectively. The XPS binding energy calibration and peak fitting were performed using the CasaXPS software. The room temperature carrier concentration (n) and mobility (μ) were measured using the Van der Pauw method (RnX Scanning Unit, Cryogenic) in a magnetic field (3 to 8 Tesla). The electrical conductivity and the Seebeck coefficient of the disk samples were measured using a commercial thermoelectric measurement system (LSR-3/110, Linseis) with an uncertainty of 5 %. The thermal diffusivities were measured in an argon-flow atmosphere using the laser flash diffusivity method using LFA-457 (NETZSCH) equipment with an uncertainty of 4 %. The specific heat capacity (C_p) was

calculated using the Dulong-Petit law. The thermal conductivity was calculated using the equation $\kappa = C_p D \lambda$, where D is the density, C_p is the specific heat capacity and λ is the thermal diffusivity.

2.3. Calculations

The configurational entropy (ΔS_{mix}) of the $(\text{Ti}_{0.33}\text{Zr}_{0.33}\text{Hf}_{0.33})_{1-x}(\text{V}_{0.33}\text{Nb}_{0.33}\text{Ta}_{0.33})_x\text{CoSb}$ HH compounds is given by:

$$\Delta S_{mix} = -R \left[\left(\sum_{i=1}^N c_i \ln c_i \right)_{X\text{-site}} + \left(\sum_{j=1}^N c_j \ln c_j \right)_{Y\text{-site}} + \left(\sum_{k=1}^N c_k \ln c_k \right)_{Z\text{-site}} \right] \quad (1)$$

where c_i , c_j , and c_k represent the mole fraction of elements present on the X, Y, and Z sites, respectively, and R is the universal gas constant. Based on the calculated ΔS_{mix} , materials are defined as high entropy ($> 1.5R$), medium entropy (1 to $1.5R$), and low entropy ($< 1R$) [32].

VEC is the total number of valence electrons, which is calculated by:

$$VEC = \sum_{i=1}^n c_i (VEC_i) \quad (2)$$

where c_i and VEC_i are atomic percentage fraction and VEC of the i^{th} element [31].

The temperature exponent (p) is calculated based on the assumption that the electrical conductivity and lattice thermal conductivity have a power law dependence on temperature:

$$\sigma = AT^p \quad \kappa_L = AT^p \quad (3)$$

where σ is the electrical conductivity, κ_L is the lattice thermal conductivity, A is a constant value, T is the absolute temperature, and p is the temperature exponent.

The density of states effective mass (m^*) and Lorenz number (L) are calculated according to the following equations [33]:

$$\alpha = \pm \frac{k_B}{e} \left(\frac{\left(r + \frac{5}{2} \right) F_{r+\frac{3}{2}}(\eta)}{\left(r + \frac{3}{2} \right) F_{r+\frac{1}{2}}(\eta)} - \eta \right) \quad (4)$$

$$F_n(\eta) = \int_0^{\infty} \frac{x^n}{1 + e^{x-\eta}} dx \quad (5)$$

$$m^* = \frac{\hbar^2}{2k_B T} \left[\frac{n}{4\pi F_{1/2}(\eta)} \right]^{3/2} \quad (6)$$

$$L = \left(\frac{k_B}{e} \right)^2 \left(\frac{\left(r + \frac{7}{2} \right) F_{r+\frac{5}{2}}(\eta)}{\left(r + \frac{3}{2} \right) F_{r+\frac{1}{2}}(\eta)} - \left[\frac{\left(r + \frac{5}{2} \right) F_{r+\frac{3}{2}}(\eta)}{\left(r + \frac{3}{2} \right) F_{r+\frac{1}{2}}(\eta)} \right]^2 \right) \quad (7)$$

Where η is the reduced Fermi energy, $F_n(\eta)$ is the n^{th} order Fermi integral, k_B is the Boltzmann constant, e is the electron charge, \hbar is the Planck constant, and r is the scattering factor. The scattering factor (r) is typically taken as $-1/2$ for acoustic phonon scattering, which is independent of the grain size and is generally assumed to be the main scattering mechanism for highly doped samples [34].

The electronic thermal conductivity κ_E was calculated using the Wiedemann-Franz law:

$$\kappa_E = LT\sigma \quad (8)$$

where L is the Lorenz number, T is the absolute temperature, and σ is the electrical conductivity.

The lattice thermal conductivity κ_L was calculated using:

$$\kappa_L = \kappa - \kappa_E \quad (9)$$

where κ is the thermal conductivity and κ_E is the electronic thermal conductivity.

The radius difference (δ_R) of the atoms was quantified using:

$$\delta_R = \sqrt{\sum_{i=1}^n c_i \left(1 - \frac{r_i}{\bar{r}_i}\right)^2} \quad (10)$$

where $\bar{r}_i = \sum_{i=1}^n c_i r_i$, with c_i and r_i being the atomic percentage fraction and atomic radius of the elements on the X site, respectively [35].

The mass difference (δ_M) was calculated using:

$$\delta_M = \sqrt{\sum_{i=1}^n c_i \left(1 - \frac{m_i}{\bar{m}_i}\right)^2} \quad (11)$$

where $\bar{m}_i = \sum_{i=1}^n c_i m_i$, with c_i and m_i being the atomic percentage fraction and atomic mass of the elements on the X site, respectively [36].

3. Results and discussion

3.1. High configurational entropy stabilized half-Heusler compounds

Table 1 shows the composition, ΔS_{mix} , and VEC of the multi-component HH compounds. The nominal composition of the multi-component HH compounds have equimolar amounts of the group IVB (Ti, Zr, and Hf) and VB (V, Nb, and Ta) elements, respectively, with a chemical formula of $(\text{Ti}_{0.33}\text{Zr}_{0.33}\text{Hf}_{0.33})_{1-x}(\text{V}_{0.33}\text{Nb}_{0.33}\text{Ta}_{0.33})_x\text{CoSb}$, abbreviated as $\text{IVB}_{1-x}\text{VB}_x\text{CoSb}$ ($x = 0.5$ to 0.75). $\text{IVB}_{0.5}\text{VB}_{0.5}\text{CoSb}$ (VEC = 18.5) was prepared as a reference composition to compare with our previous work [24]. The VEC and charge carrier concentration can be changed by changing the ratio of the group IVB to VB element. Even with these changes in composition, all of the samples can still be classified as HEHH compounds, exhibiting ΔS_{mix} exceeding 1.5R.

Fig. 1 shows the XRD patterns of the HEHH powders after ball milling and SPS processing (crushed sample), which exhibit a single-phase cubic structure with a space group of $F43m$ [24]. SEM and EDS analysis were conducted to further verify the phase purity of the HEHH samples. As shown in Fig. 2a, the fracture surface of the $\text{IVB}_{0.5}\text{VB}_{0.5}\text{CoSb}$ compound exhibits a well sintered microstructure with clear grain boundaries, consistent with the high-density values ($\sim 95\%$) presented in Fig. S2 in the Supporting Information. The sample comprises large grains of approximately 1 μm in size, with smaller grains (around 0.1 μm) surrounding them. The EDS point analysis shown in Fig. 2b confirms the nominal composition. Similarly, for the other HEHH compounds, the actual compositions, determined as the average values of three EDS point analysis, are presented in Table S1 (Supporting Information), and are similar to the nominal compositions within the accuracy of EDS analysis. A backscattered electron (BSE) image of a well-polished surface is shown in Fig. 2c. A homogeneous element distribution is also confirmed by EDS mapping (Fig. 2c). Higher resolution BSE images with EDS mapping of $\text{IVB}_{0.5}\text{VB}_{0.5}\text{CoSb}$ are also presented in Fig. S3 (Supporting Information), confirming the homogeneity of the sample. Additionally, $\text{IVB}_{0.25}\text{VB}_{0.75}\text{CoSb}$, which has the greatest potential for

Table 1

Composition, abbreviation, configurational entropy (ΔS_{mix}), and valence electron counts (VEC) of high-entropy half-Heusler compounds.

Composition	Abbreviation ($\text{IVB}_{1-x}\text{VB}_x\text{CoSb}$)	ΔS_{mix}	VEC
$(\text{Ti}_{0.33}\text{Zr}_{0.33}\text{Hf}_{0.33})_{0.5}(\text{V}_{0.33}\text{Nb}_{0.33}\text{Ta}_{0.33})_{0.5}\text{CoSb}$	$\text{IVB}_{0.5}\text{VB}_{0.5}\text{CoSb}$	1.792R	18.5
$(\text{Ti}_{0.33}\text{Zr}_{0.33}\text{Hf}_{0.33})_{0.44}(\text{V}_{0.33}\text{Nb}_{0.33}\text{Ta}_{0.33})_{0.56}\text{CoSb}$	$\text{IVB}_{0.44}\text{VB}_{0.56}\text{CoSb}$	1.786R	18.56
$(\text{Ti}_{0.33}\text{Zr}_{0.33}\text{Hf}_{0.33})_{0.4}(\text{V}_{0.33}\text{Nb}_{0.33}\text{Ta}_{0.33})_{0.6}\text{CoSb}$	$\text{IVB}_{0.4}\text{VB}_{0.6}\text{CoSb}$	1.772R	18.6
$(\text{Ti}_{0.33}\text{Zr}_{0.33}\text{Hf}_{0.33})_{0.35}(\text{V}_{0.33}\text{Nb}_{0.33}\text{Ta}_{0.33})_{0.65}\text{CoSb}$	$\text{IVB}_{0.35}\text{VB}_{0.65}\text{CoSb}$	1.746R	18.65
$(\text{Ti}_{0.33}\text{Zr}_{0.33}\text{Hf}_{0.33})_{0.3}(\text{V}_{0.33}\text{Nb}_{0.33}\text{Ta}_{0.33})_{0.7}\text{CoSb}$	$\text{IVB}_{0.3}\text{VB}_{0.7}\text{CoSb}$	1.709R	18.7
$(\text{Ti}_{0.33}\text{Zr}_{0.33}\text{Hf}_{0.33})_{0.25}(\text{V}_{0.33}\text{Nb}_{0.33}\text{Ta}_{0.33})_{0.75}\text{CoSb}$	$\text{IVB}_{0.25}\text{VB}_{0.75}\text{CoSb}$	1.661R	18.75

exhibiting phase separation or elemental local clustering due to its largest composition difference compared to $\text{IVB}_{0.5}\text{VB}_{0.5}\text{CoSb}$ and lowest ΔS_{mix} of HEHH compounds, was also studied, and there is no evidence of phase separation or elemental local clustering (Fig. S4, Supporting Information).

3.2. Chemical states and bonding features of $\text{IVB}_{1-x}\text{VB}_x\text{CoSb}$ compounds

The chemical states and bonding characteristics of the $\text{IVB}_{1-x}\text{VB}_x\text{CoSb}$ samples were investigated using XPS. Fig. 3 presents the XPS spectra showing the intensity as a function of binding energy, with the C–C peak at 284.8 eV used for energy calibration. The spectra for cobalt (Co 2p), antimony (Sb 2p), vanadium (V 2p), titanium (Ti 2p), niobium (Nb 3d), zirconium (Zr 3d), tantalum (Ta 4f), and hafnium (Hf 4f) are indexed in Fig. 3a, and the corresponding high-resolution spectra and peak fitting for each element are shown in Fig. 3b–3i. However, Fig. 3c also reveals a distinct O 1s peak near 531 eV, consistent with previous research by Zhu *et al.* on $\text{Nb}_{0.8}\text{CoSb}$ [37]. This peak confirms the presence of surface oxidation and hydroxyl (OH) groups [38], which likely originate from the water used during the polishing process, indicating surface contamination rather than inherent chemical bonding within the $\text{IVB}_{1-x}\text{VB}_x\text{CoSb}$ samples.

In Fig. 3d–3i, the XPS peak positions of the group IVB (Ti 2p, Zr 3d, and Hf 4f) and group VB (V 2p, Nb 3d, and Ta 4f) elements do not change with composition changes. However, in Fig. 3b, the peak of Co 2p shifts from 777.26 eV for $\text{IVB}_{0.5}\text{VB}_{0.5}\text{CoSb}$ to 777.55 eV for $\text{IVB}_{0.25}\text{VB}_{0.75}\text{CoSb}$. A similar peak shift can also be observed for Sb 2p in Fig. 3c. The shift of the main peaks of Co 2p and Sb 2p to higher energy with an increasing ratio of group VB elements is associated with stronger polar bonding and lower μ , which is consistent with our μ results in Fig. S5 (Supporting Information), reported by Zheng *et al.* in Zn–Sb thin films [39]. The stronger polar bonding observed with increasing ratio of group VB elements can be attributed to their higher electronegativity compared to the IVB elements, resulting in lower μ . Additionally, the peak intensity was utilized to illustrate the changes in the element content. As shown in Fig. 3d, 3e, and 3f, the intensity of the Ti 2p, Zr 3d, and Hf 4f peaks decrease with the reduction of group IVB elements, while the narrow scans of V 2p, Nb 3d, and Ta 4f presented in Fig. 3g, 3h, and 3i show an increasing peak intensity with the increase of group VB elements, which follows the trend based on the nominal compositions.

3.3. Temperature dependence of electrical properties

The σ , α , PF , and m^* of the HEHHs are shown in Fig. S6 (Supporting Information). The m^* was estimated to range from 2.4 m_e to 4.1 m_e with increasing x , which is smaller than the value of 6.3 m_e reported for $(\text{Hf}_{0.3}\text{Zr}_{0.7})_{1-x}\text{Nb}_x\text{CoSb}$ [40]. In Fig. 4, S7, and S8, the $\sigma(T)$, $\alpha(T)$, and $PF(T)$ of the HEHH materials are compared with medium- and low-entropy counterparts with different VEC from 17.8 to 19 [24, 41–47]. Regardless of changes in entropy and VEC, the magnitude of the α of all of HHs, including HEHHs, maintain a positive temperature dependence, typical of highly doped metallic-like transport behavior. In Fig. 4, the σ of n-type HEHHs exhibits a positive (semiconducting) temperature dependence, which is not consistent with metallic behavior. This point is discussed further below.

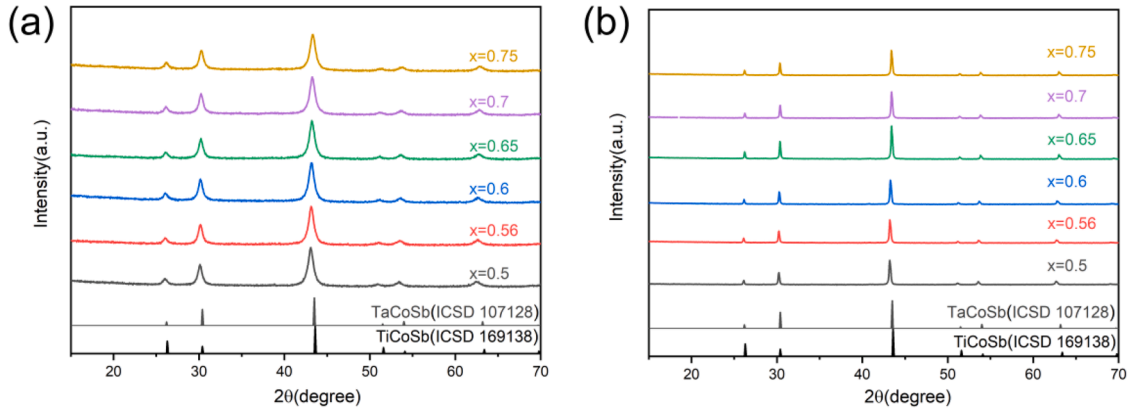


Fig. 1. Powder XRD patterns of high-entropy $IVB_{1-x}VB_xCoSb$ ($x = 0.5$ to 0.75) compounds (a) ball milling (b) SPS (crushed sample).

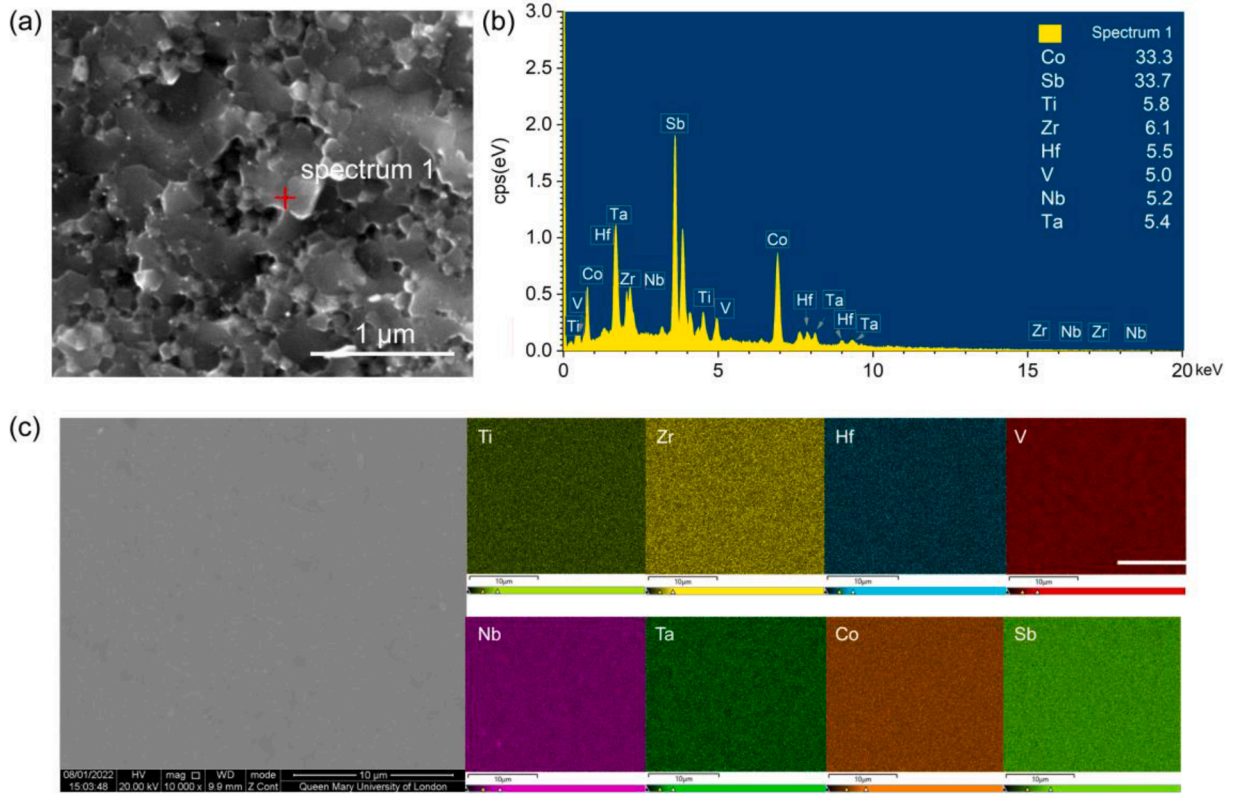


Fig. 2. (a) SEM fracture image (b) EDS elemental analysis (c) Back-scattered electron image and EDS mapping of $IVB_{0.5}VB_{0.5}CoSb$ sample.

Fig. 5 shows the σ and p for $V_{0.95}CoSb$ [44], $Ti_{0.25}V_{0.75}CoSb$ [45], and $IVB_{1-x}VB_xCoSb$. The calculated temperature exponent p is small and positive (+0.29 to +0.76) for the high entropy $IVB_{1-x}VB_xCoSb$ compositions, whereas it is negative for the low entropy $Ti_{0.25}V_{0.75}CoSb$ (-0.33) and $V_{0.95}CoSb$ (-0.79) compositions. Note that $V_{0.95}CoSb$, $Ti_{0.25}V_{0.75}CoSb$, and $IVB_{0.25}VB_{0.75}CoSb$ all have a VEC value of 18.75 but exhibit different ΔS_{mix} of 0.05R, 0.56R, and 1.66R, respectively. The differences in p indicate different scattering mechanisms.

Among the well-studied charge carrier scattering mechanisms, the p of acoustic phonon scattering (APS) [40] ($\sim T^{-1.5}$), polar optical phonon scattering (OPS) [48] ($\sim T^{-0.75}$), and alloy scattering (AS) [49] ($\sim T^{-0.5}$) are all negative. Grain boundary scattering (GBS) and ionized impurity scattering (IIS) exhibit positive p at low temperatures [34,50,51]. To distinguish GBS and IIS, Hu *et al.* proposed the ratio, α_{BD} , between the effective Bohr radius (a_B^*) and Debye screening length (L_D):

$$\alpha_{BD} = \frac{a_B^*}{L_D} = \frac{4\pi\hbar}{m_b^*e} \sqrt{\frac{\epsilon n}{N_v k_B T}} \quad (12)$$

where the \hbar is the reduced Planck constant, m_b^* is the band effective mass, e is the electron charge, ϵ is the dielectric constant, n is the carrier concentration, N_v is the valley degeneracy, and T is the absolute temperature. If $\alpha_{BD} > 1$, IIS can be excluded, and GBS is the dominant scattering mechanism. If $\alpha_{BD} < 1$, both IIS and GBS might occur, but if $\alpha_{BD} \ll 1$ then it is dominated by IIS [50].

Assuming the N_v and ϵ of the HEHH compounds are the same as for $ZrCoSb$ ($N_v = 3$, $\epsilon = 19$, shown in ref 50), α_{BD} for $IVB_{0.25}VB_{0.75}CoSb$ ($m_b^* = 4.1 m_e$, $n = 7 \times 10^{20} \text{ cm}^{-3}$) and $IVB_{0.5}VB_{0.5}CoSb$ ($m_b^* = 2.4 m_e$, $n = 2.1 \times 10^{20} \text{ cm}^{-3}$) are 0.73 and 0.69, respectively. Therefore, both IIS and GBS might occur in HEHH compounds due to their α_{BD} values being slightly less than 1. In heavily doped HHs with high n ($> 10^{19} \sim 10^{21}$

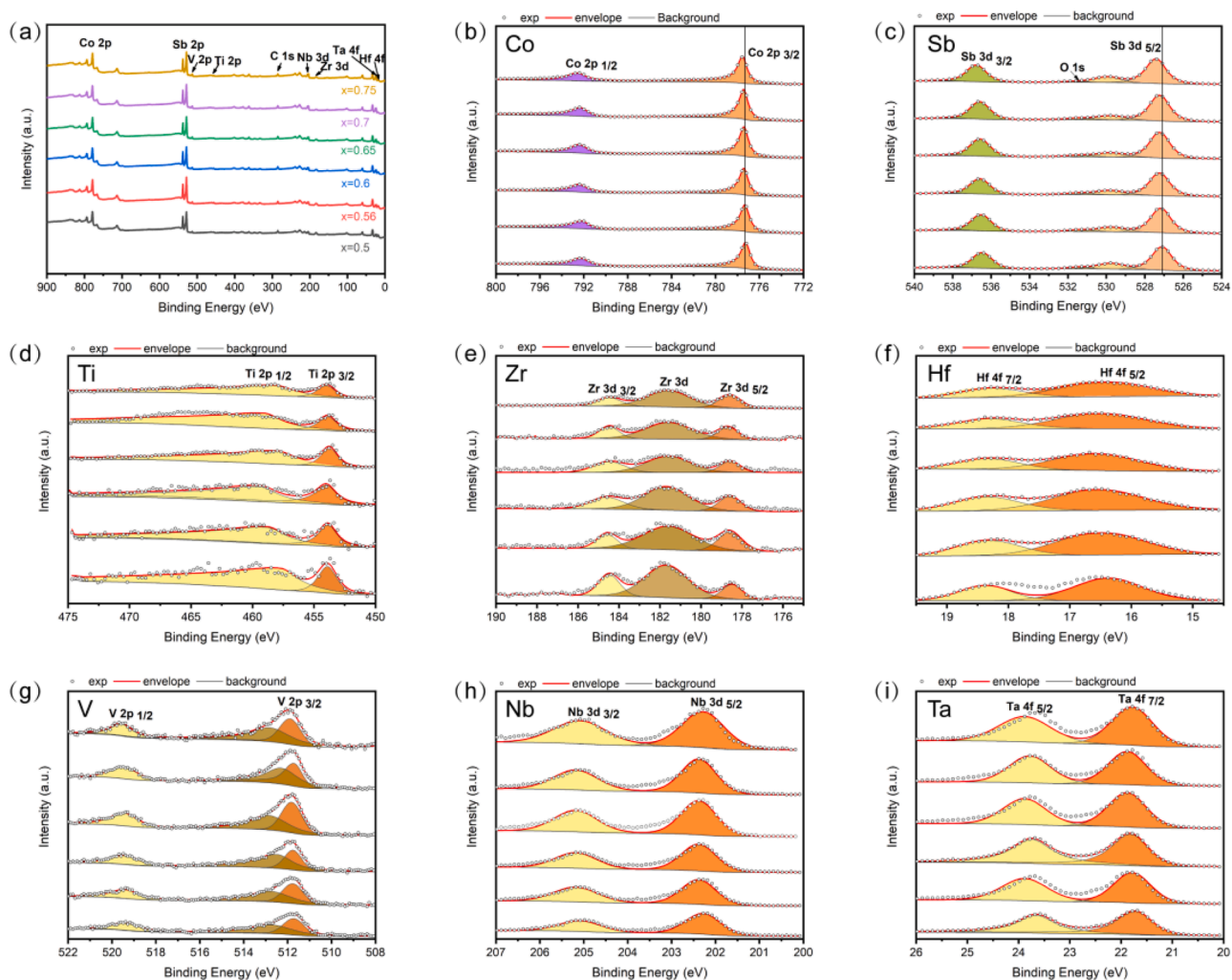


Fig. 3. (a) XPS survey, (b) Co 2p, (c) Sb 2p, (d) Ti 2p, (e) Zr 3d, (f) Hf 4f, (g) V 2p, (h) Nb 3d, and (i) Ta 4f scans of $IVB_{1-x}VB_xCoSb$ ($x = 0.5$ to 0.75).

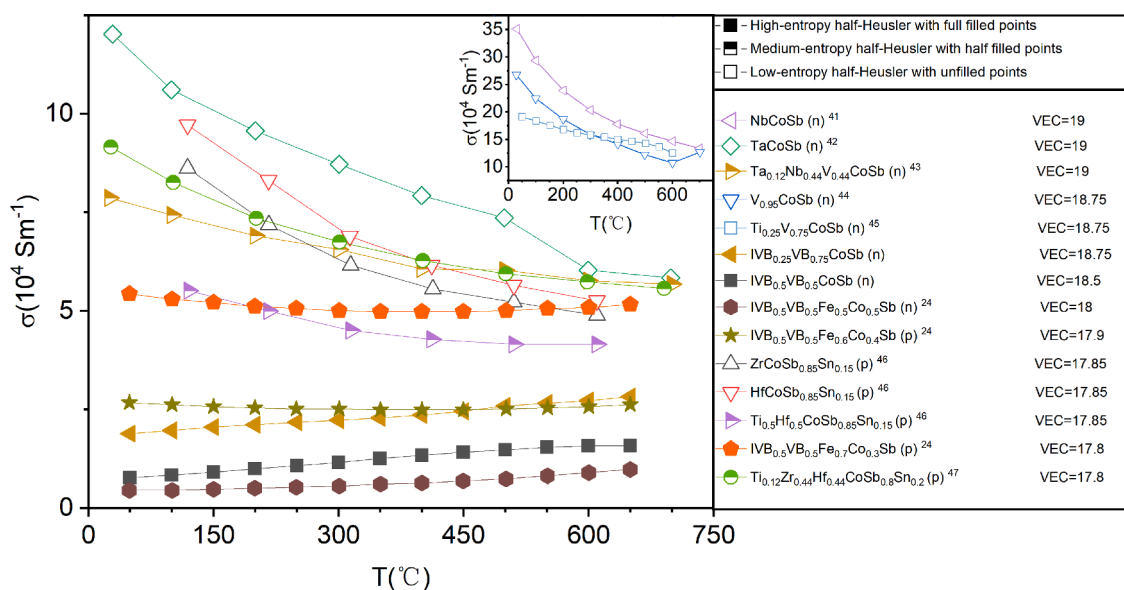


Fig. 4. Temperature-dependent electrical conductivity of high-entropy (full-filled data points), medium-entropy (half-filled data points), and low-entropy (unfilled data points) XCoSb half-Heusler compounds.

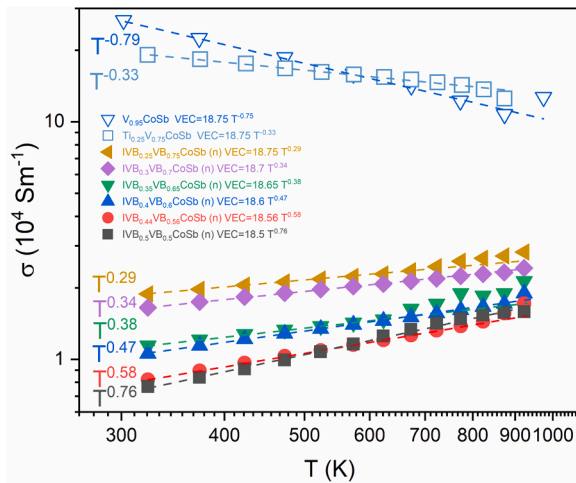


Fig. 5. Temperature exponent p of electrical conductivity for low- ($V_{0.95}CoSb^{44}$ and $Ti_{0.25}V_{0.75}CoSb^{45}$) and high-entropy ($IVB_{1-x}VB_xCoSb$, $x = 0.5$ to 0.75) half-Heusler compounds. The high-entropy compositions are labeled with full-filled data points and low-entropy compositions are labeled with unfilled data points.

cm^{-3}), the ionic impurities are typically screened [34], and GBS is the most likely scattering mechanism for the materials with thermally-activated $\sigma(T)$, such as for $ZrCoSb$ ($\alpha_{BD} = 0.6$, grain size $< 5 \mu m$, and $n = 4 \times 10^{20} cm^{-3}$) [40] and $NbFeSb$ ($\alpha_{BD} = 1.2$, grain size $= 0.3 \sim 4.5 \mu m$, and $n = 8 \times 10^{20} cm^{-3}$) [52]. However, for the HEHH $IVB_{1-x}VB_xCoSb$ samples, the magnitude of the σ increased and the p decreased (0.76 to 0.29) with increasing VEC (Fig. 5). These changes occur in samples with similar grain size (small grain size = 100 nm, large grain size = 1 μm), suggesting that GBS may not be the main scattering mechanism. Also inconsistent with GBS, we do not observe the typical transition to APS at elevated temperature. Our work therefore usefully highlights that the transport and scattering mechanisms in these complex high-entropy systems is still an open question, which may stimulate further research.

It is noteworthy that p-type HEHH compounds with VEC below 18 also have small values of p , as shown in Fig. S9 (Supporting Information). $ZrCoSb_{0.8}Sn_{0.2}$ [53], $HfCoSb_{0.8}Sn_{0.2}$ [53], $Ti_{0.12}Zr_{0.44}Hf_{0.44}CoSb_{0.8}Sn_{0.2}$ [47], and $IVB_{0.5}VB_{0.5}Fe_{0.7}Co_{0.3}Sb$ [24] have the same VEC of 17.8 but different ΔS_{mix} (0.5R, 0.5R, 1.48R, and 2.4R, respectively). The p decreases with increasing ΔS_{mix} , and the HEHH ($IVB_{0.5}VB_{0.5}Fe_{0.7}Co_{0.3}Sb$) exhibits the smallest p value of -0.13 below 623 K. However, the σ of $IVB_{0.5}VB_{0.5}Fe_{0.7}Co_{0.3}Sb$ exhibits a positive trend above 723 K, which is attributed to the bipolar effect [24].

To investigate the effect of composition variation on the n in multi-component HEHH compounds, the measured values are compared with the theoretical values as presented in Fig. 6. The data for n comes from Fig. S5 (Supporting Information). The relative carrier concentration efficiency was calculated assuming that each relative composition changing atom supplies exactly one carrier. HEHH with a composition of $IVB_{0.25}VB_{0.75}CoSb$ has the smallest relative carrier concentration efficiency (10 %), which is much lower compared to medium- and low-entropy HH materials (46 % for $(Hf_{0.3}Zr_{0.7})_{1-y}Nb_yCoSb$ and 77 % for $ZrCoSb_{1-y}Sn_y$) [40,54]. The low carrier concentration efficiency indicates that HEHH compounds are less sensitive to composition changes on the X site. Given that the HEHH samples are pure and possess the correct compositions according to EDS, the low carrier concentration efficiency of 10 % suggests a unique behavior in high-entropy materials that deserves further investigation in both high-entropy half-Heusler and other high-entropy materials.

3.4. High-entropy effect on thermal properties

The $\kappa(T)$, $\kappa_E(T)$, $\kappa_L(T)$, $L(T)$, and ZT of HEHs are shown in Fig. S10

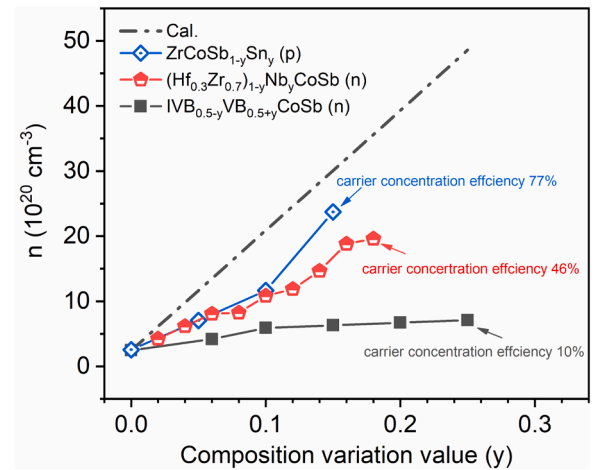


Fig. 6. Room temperature carrier concentration versus composition variation value (y) for $ZrCoSb_{1-y}Sn_y^{54}$, $(Hf_{0.3}Zr_{0.7})_{1-y}Nb_yCoSb^{40}$, and $IVB_{0.5-y}VB_{0.5+y}CoSb$ compounds. The dash lines were calculated assuming that each relative composition changing atom supplies exactly one carrier. The high-entropy composition is labeled with full-filled data points, medium-entropy composition is labeled with half-filled data points, and low-entropy composition is labeled with unfilled data points.

and S11a (Supporting Information). It is widely known that multi-component materials with significant mass and strain contrast tend to exhibit enhanced phonon scattering and reduced κ . High-entropy materials provide a promising avenue for maximizing this effect, owing to the concept of entropy stabilization, which facilitates a greater number of multi-component constituents and the possibility to select diverse elements. Thus, studying the high-entropy effect on thermal properties is of great interest. In Fig. 7, the κ_L of HEHH compounds are compared with medium- and low-entropy HH samples. The low-entropy samples, which only contain one element (such as Ti, Zr, Hf, V, and Nb) on the X site, have much higher κ_L . However, there is a significant reduction in κ_L in the medium- and high-entropy samples due to the large atomic radius and mass differences in multi-component systems. Table 2 presents the ΔS_{mix} , δ_R , and δ_M on the X site, and the room-temperature κ_L of XCoSb-based HH compounds. Among them, the $IVB_{0.44}VB_{0.56}CoSb$ sample exhibits the largest δ_R of 0.054, which is twice that of $(Zr_{0.4}Hf_{0.6})_{0.88}Nb_{0.12}CoSb$ (0.025). $IVB_{0.44}VB_{0.56}CoSb$ also exhibits the largest δ_M of 0.506. Notably, due to its significant differences in radius

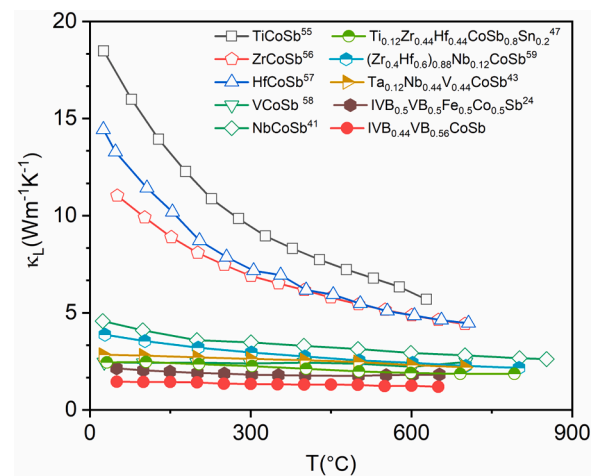


Fig. 7. The lattice thermal conductivities κ_L of XCoSb based HH compounds. The high-entropy compositions are labeled with full-filled data points, medium-entropy compositions are labeled with half-filled data points, and low-entropy compositions are labeled with unfilled data points.

Table 2

Composition, configurational entropy value ΔS_{mix} (R), radius difference δ_R and mass difference δ_M on the X site and room-temperature lattice thermal conductivities κ_L ($\text{W}\cdot\text{m}^{-1}\cdot\text{K}^{-1}$) of XCoSb based HH.

Composition	ΔS_{mix}	δ_R	δ_M	κ_L
TiCoSb ⁵⁵	–	–	–	18.46
ZrCoSb ⁵⁶	–	–	–	11.02
HfCoSb ⁵⁷	–	–	–	14.43
NbCoSb ⁴¹	–	–	–	4.57
(Zr _{0.4} Hf _{0.6}) _{0.88} Nb _{0.12} CoSb ⁵⁹	0.959	0.025	0.343	3.87
Ti _{0.12} Zr _{0.44} Hf _{0.44} CoSb _{0.8} Sn _{0.2} ⁴⁷	1.477	0.024	0.4	2.45
IVB _{0.44} VB _{0.56} CoSb	1.786	0.054	0.506	1.46

and mass, the κ_L of IVB_{0.44}VB_{0.56}CoSb reaches a record-low value of 1.19 $\text{W}\cdot\text{m}^{-1}\cdot\text{K}^{-1}$ at 650 °C, surpassing the values observed in other XCoSb HH materials [24,41,43,47,55–59].

Fig. 8 shows the $\kappa_L(T)$ and p of low-, medium-, and high-entropy HH samples, which provides further insight into the multicomponent high-entropy effect. Compounds containing large amounts of vanadium, such as VCoSb and Ti_{0.12}Hf_{0.44}V_{0.44}CoSb, were not included due to the instability of vanadium with its complex oxidation states. The low-entropy compounds, TiCoSb and HfCoSb, exhibit a $\kappa_L \propto T^{-1}$ relationship, indicative of typical Umklapp scattering [60]. NbCoSb and (Zr_{0.4}Hf_{0.6})_{0.88}Nb_{0.12}CoSb show a p close to -0.5 , suggesting strong alloy scattering [61]. While HEHs, such as IVB_{0.5}VB_{0.5}Fe_{0.5}Co_{0.5}Sb ($\sim T^{-0.25}$) and IVB_{0.44}VB_{0.56}CoSb ($\sim T^{-0.18}$), exhibit much lower p compared to their low- and medium-entropy counterparts, suggesting possible mixed scattering involving Umklapp scattering, strong alloying scattering with large radius and mass difference, and grain boundary scattering. It is noteworthy that increased scattering in HEHs impacts both phonon and electron transport. Compared with the well-studied HH compositions (TiZrHf)Co(SbSn) [30,47], the lowest κ_L of the HEHs has decreased by 36 %, from 1.85 $\text{W}\cdot\text{m}^{-1}\cdot\text{K}^{-1}$ to 1.19 $\text{W}\cdot\text{m}^{-1}\cdot\text{K}^{-1}$ (Fig. 7). However, the peak PF has decreased by 57 %, from 2.87 $\text{mW}\cdot\text{m}^{-1}\cdot\text{K}^{-2}$ to 1.21 $\text{mW}\cdot\text{m}^{-1}\cdot\text{K}^{-2}$ (Fig. S8, Supporting Information).

Finally, the highest ZT of 0.4 was achieved in IVB_{0.35}VB_{0.65}CoSb at 650 °C (shown in Fig. S11a, Supporting Information), which was improved by 33 % compared with the reference IVB_{0.5}VB_{0.5}CoSb compound. The reproducibility of σ , α , PF , and κ is demonstrated in Fig. S12 (Supporting Information). These TE properties of IVB_{0.35}VB_{0.65}CoSb can be reproduced through a heating and cooling cycle, even at an elevated temperature of 750 °C, leading to an improved ZT value of 0.45 shown in Fig. S11b (Supporting Information).

4. Conclusions

Single phase compositions IVB_{1-x}VB_xCoSb (IVB = equimolar Ti, Zr, Hf and VB = equimolar V, Nb, Ta) with x in the range 0.5 to 0.75 were synthesised and densified to high density (>95 %). Their σ shows a low and positive temperature dependence ($p = +0.29$ for IVB_{0.25}VB_{0.75}CoSb) compared to low- and medium-entropy HH materials ($p \leq -0.33$), suggesting different scattering mechanisms. Further analysis shows that the dominant scattering mechanism of σ for these complex high-entropy systems can not simply be explained by GBS or IIS. Our work therefore usefully highlights that the transport and scattering mechanisms in these complex high-entropy systems is still an open question, which may stimulate further research. Their electrical properties also show an insensitivity to composition changes with a low carrier concentration efficiency of 10 %. They show ultralow κ_L (1.19 $\text{W}\cdot\text{m}^{-1}\cdot\text{K}^{-1}$) with a low temperature dependence ($p = -0.18$) for IVB_{0.44}VB_{0.56}CoSb with mixed phonon scattering because of large radius and mass difference, compared to low- and medium-entropy materials ($p \leq -0.32$). These results have positive implications for the development of high-entropy materials from inexpensive less pure precursors and the recyclability of material.

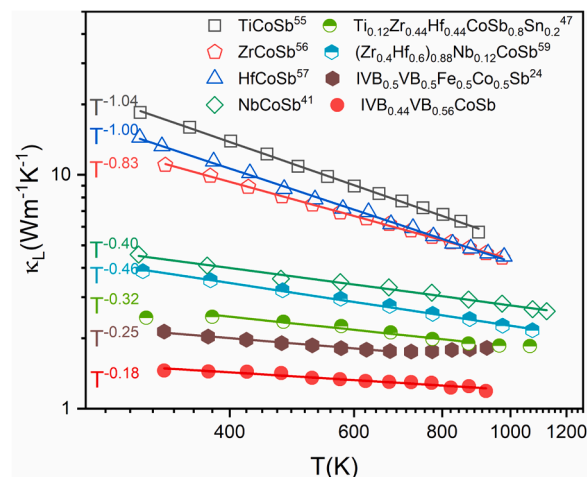


Fig. 8. Temperature exponent p of lattice thermal conductivities κ_L of XCoSb based HH compounds. The high-entropy compositions are labeled with full-filled data points, medium-entropy compositions are labeled with half-filled data points, and low-entropy compositions are labeled with unfilled data points.

Declaration of competing interest

The authors declare that they have no known competing financial interests or personal relationships that could have appeared to influence the work reported in this paper.

Acknowledgement

We wish to acknowledge European Thermodynamics Ltd and the Energy Entrepreneurs Fund project 6148 for assisting in preliminary work for this paper. S. L. thanks the financial support from China Scholarship Council (CSC; No. 202006160010). The authors also appreciate the valuable suggestions from the reviewers, which have significantly contributed to improving the analysis of the electrical properties.

Supplementary materials

Supplementary material associated with this article can be found, in the online version, at doi:10.1016/j.actamat.2024.119761.

References

- [1] G.J. Snyder, E.S. Toberer, Complex thermoelectric materials, *Nat. Mater.* 7 (2) (2008) 105–114.
- [2] X.L. Shi, J. Zou, Z.G. Chen, Advanced thermoelectric design: from materials and structures to devices, *Chem. Rev.* 120 (15) (2020) 7399–7515.
- [3] Z.H. Liu, W.H. Gao, W.H. Zhang, N. Sato, Q.S. Guo, T. Mori, High power factor and enhanced thermoelectric performance in Sc and Bi codoped GeTe: insights into the hidden role of rhombohedral distortion degree, *Adv. Energy Mater.* 10 (42) (2020) 8.
- [4] Q.H. Jiang, H.X. Yan, Y.H. Lin, Y. Shen, J.Y. Yang, M.J. Reece, Colossal thermoelectric enhancement in Cu₂+xZn_{1-x}SnS₄ solid solution by local disordering of crystal lattice and multi-scale defect engineering, *J. Mater. Chem. A* 8 (21) (2020) 10909–10916.
- [5] R. He, H.T. Zhu, J.Y. Sun, J. Mao, H. Reith, S. Chen, G. Schierning, K. Nielsch, Z. F. Ren, Improved thermoelectric performance of n-type half-Heusler MCo_{1-x}Ni_xSb (M = Hf, Zr), *Mater. Today Phys.* 1 (2017) 24–30.
- [6] Y.Z. Pei, X.Y. Shi, A. LaLonde, H. Wang, L.D. Chen, G.J. Snyder, Convergence of electronic bands for high performance bulk thermoelectrics, *Nature* 473 (7345) (2011) 66–69.
- [7] J.H. Kim, H. Cho, S.Y. Back, J.H. Yun, H.S. Lee, J.S. Rhyee, Lattice distortion and anisotropic thermoelectric properties in hot-deformed CuI-doped Bi₂Te_{2.7}Se_{0.3}, *J. Alloys. Compd.* 815 (2020) 8.
- [8] Y. Dou, J. Li, Y. Xie, X. Wu, L. Hu, F. Liu, W. Ao, Y. Liu, C. Zhang, Lone-pair engineering: achieving ultralow lattice thermal conductivity and enhanced thermoelectric performance in Al-doped GeTe-based alloys, *Mater. Today Phys.* 20 (2021) 8.

- [9] X. Fan, S. Gao, Q. Chen, D.Y. Zhou, L.J. Chang, Y. Wang, Y.W. Zhang, L. Deng, H. A. Ma, X.P. Jia, Synthesis optimization and thermoelectric properties of S-filled and Te-Se double-substituted skutterudite under high pressure, *Inorg. Chem.* 61 (21) (2022) 8144–8152.
- [10] B. Cantor, I.T.H. Chang, P. Knight, A.J.B. Vincent, Microstructural development in equiatomic multicomponent alloys, *Mater. Sci. Eng. A Struct. Mater. Prop. Microstruct. Process.* 375 (2004) 213–218.
- [11] J.W. Yeh, S.K. Chen, S.J. Lin, J.Y. Gan, T.S. Chin, T.T. Shun, C.H. Tsau, S.Y. Chang, Nanostructured high-entropy alloys with multiple principal elements: novel alloy design concepts and outcomes, *Adv. Eng. Mater.* 6 (5) (2004) 299–303.
- [12] J.W. Yeh, Recent progress in high-entropy alloys, *Annales De Chimie-Science Des Materiaux* 31 (6) (2006) 633–648.
- [13] C.M. Rost, E. Sachtel, T. Borman, A. Moballegh, E.C. Dickey, D. Hou, J.L. Jones, S. Curtarolo, J.P. Maria, Entropy-stabilized oxides, *Nat. Commun.* 6 (2015) 8.
- [14] E. Castle, T. Csanadi, S. Grasso, J. Dusza, M. Reece, Processing and properties of high-entropy ultra-high temperature carbides, *Sci. Rep.* 8 (2018) 12.
- [15] Y.C. Wang, T. Csanadi, H.F. Zhang, J. Dusza, M.J. Reece, Synthesis, microstructure, and mechanical properties of novel high entropy carbonitrides, *Acta Mater.* 231 (2022) 9.
- [16] S. Barbarossa, R. Orru, G. Cao, A. Balbo, F. Zanotto, E. Sani, Optical properties of bulk high-entropy diborides for solar energy applications, *J. Alloys. Compd.* 935 (2023) 9.
- [17] D. Moskovskikh, S. Vorotilo, V. Buinevich, A. Sedegov, K. Kuskov, A. Khort, C. Shuck, M. Zhukovskiy, A. Mukasyan, Extremely hard and tough high entropy nitride ceramics, *Sci. Rep.* 10 (1) (2020) 8.
- [18] R.Z. Zhang, F. Gucci, H.Y. Zhu, K. Chen, M.J. Reece, Data-driven design of ecofriendly thermoelectric high-entropy sulfides, *Inorg. Chem.* 57 (20) (2018) 13027–13033.
- [19] C.R. McCormick, R.E. Schaak, Simultaneous multication exchange pathway to high-entropy metal sulfide nanoparticles, *J. Am. Chem. Soc.* 143 (2) (2021) 1017–1023.
- [20] J.X. Yang, B.H. Dai, C.Y. Chiang, I.C. Chiu, C.W. Pao, S.Y. Lu, I.Y. Tsao, S.T. Lin, C. T. Chiu, J.W. Yeh, P.C. Chang, W.H. Hung, Rapid fabrication of high-entropy ceramic nanomaterials for catalytic reactions, *ACS. Nano* 15 (7) (2021) 12324–12333.
- [21] L. Lin, K. Wang, A. Sarkar, C. Njel, G. Karkera, Q.S. Wang, R. Azmi, M. Fichtner, H. Hahn, S. Schweidler, B. Breitung, High-entropy sulfides as electrode materials for Li-Ion batteries, *Adv. Energy Mater.* 12 (8) (2022) 11.
- [22] T. Jin, X.H. Sang, R.R. Unocic, R.T. Kinch, X.F. Liu, J. Hu, H.L. Liu, S. Dai, Mechanochemical-assisted synthesis of high-entropy metal nitride via a soft urea strategy, *Adv. Mater.* 30 (23) (2018) 8.
- [23] B.B. Jiang, Y. Yu, J. Cui, X.X. Liu, L. Xie, J.C. Liao, Q.H. Zhang, Y. Huang, S.C. Ning, B.H. Jia, B. Zhu, S.Q. Bai, L.D. Chen, S.J. Pennycook, J.Q. He, High-entropy-stabilized chalcogenides with high thermoelectric performance, *Science* (1979) 371 (6531) (2021) 830. ++.
- [24] K. Chen, R.Z. Zhang, J.W.G. Bos, M.J. Reece, Synthesis and thermoelectric properties of high-entropy half-Heusler $MFe_{1-x}Co_xSb$ ($M = \text{equimolar Ti, Zr, Hf, V, Nb, Ta}$), *J. Alloys. Compd.* 892 (2022) 7.
- [25] J.F. Cai, J.X. Yang, G.Q. Liu, H.X. Wang, F.F. Shi, X.J. Tan, Z.H. Ge, J. Jiang, Ultralow thermal conductivity and improved ZT of $CuNiTe_2$ by high-entropy structure design, *Mater. Today Phys.* 18 (2021) 8.
- [26] Z.H. Lou, P. Zhang, J.T. Zhu, L.Y. Gong, J. Xu, Q. Chen, M.J. Reece, H.X. Yan, F. Gao, A novel high-entropy perovskite ceramics $Sr_{0.9}La_{0.1}(Zr_{0.25}Sn_{0.25}Ti_{0.25}Hf_{0.25})O_{-3}$ with low thermal conductivity and high Seebeck coefficient, *J. Eur. Ceram. Soc.* 42 (8) (2022) 3480–3488.
- [27] P.J. Wang, H.J. Kang, X. Yang, Y. Liu, C. Cheng, T.M. Wang, Inhibition of lattice thermal conductivity of ZrNiSn-based Half-Heusler Thermoelectric materials by entropy adjustment, *J. Inorg. Mater.* 37 (7) (2022) 717–723.
- [28] J.X. Yang, J.F. Cai, R.Y. Wang, Z. Guo, X.J. Tan, G.Q. Liu, Z.H. Ge, J. Jiang, Entropy engineering realized ultralow thermal conductivity and high seebeck coefficient in lead-free SnTe, *ACS. Appl. Energy Mater.* 4 (11) (2021) 12738–12744.
- [29] P. Zhang, Z.H. Lou, L.Y. Gong, J. Xu, Q. Chen, M.J. Reece, H.X. Yan, Z. Dashevsky, F. Gao, High-entropy $MTiO_3$ perovskite oxides with glass-like thermal conductivity for thermoelectric applications, *J. Alloys. Compd.* 937 (2023) 12.
- [30] R.J. Quinn, J.-W.G. Bos, Advances in half-Heusler alloys for thermoelectric power generation, *Mater. Adv.* 2 (19) (2021) 6246–6266.
- [31] W.G. Zeier, J. Schmitt, G. Hautier, U. Aydemir, Z.M. Gibbs, C. Felser, G.J. Snyder, Engineering half-Heusler thermoelectric materials using Zintl chemistry, *Nat. Rev. Mater.* 1 (6) (2016) 10.
- [32] B.S. Murty, J.-W. Yeh, S. Ranganathan, P. Bhattacharjee, High-entropy alloys, *Elsevier* 2019.
- [33] D. Zhang, J.Y. Yang, H.C. Bai, Y.B. Luo, B. Wang, S.H. Hou, Z.L. Li, S.F. Wang, Significant average ZT enhancement in Cu_3SbSe_4 -based thermoelectric material via softening p-d hybridization, *J. Mater. Chem. A* 7 (29) (2019) 17648–17654.
- [34] Q. Ren, C. Fu, Q. Qiu, S. Dai, Z. Liu, T. Masuda, S. Asai, M. Hagihala, S. Lee, S. Torri, Establishing the carrier scattering phase diagram for ZrNiSn-based half-Heusler thermoelectric materials, *Nat. Commun.* 11 (1) (2020) 3142.
- [35] H.Q. Song, F.Y. Tian, Q.M. Hu, L. Vitos, Y.D. Wang, J. Shen, N.X. Chen, Local lattice distortion in high-entropy alloys, *Phys. Rev. Mater.* 1 (2) (2017) 8.
- [36] D. Song, T. Song, U. Paik, G. Lyu, Y.G. Jung, H.B. Jeon, Y.S. Oh, Glass-like thermal conductivity in mass-disordered high-entropy (Y, Yb)(2)(Ti, Zr, Hf)(2)O-7 for thermal barrier material, *Mater. Des.* 210 (2021) 10.
- [37] K.Y. Xia, P.F. Nan, S.H. Tan, Y.M. Wang, B.H. Ge, W.Q. Zhang, S. Anand, X.B. Zhao, G.J. Snyder, T.J. Zhu, Short-range order in defective half-Heusler thermoelectric crystals, *Energy Environ. Sci.* 12 (5) (2019) 1568–1574.
- [38] T.L. Barr, ESCA study of termination of passivation of elemental metals, *J. Phys. Chem.* 82 (16) (1978) 1801–1810.
- [39] Z.H. Zheng, P. Fan, P.J. Liu, J.T. Luo, X.M. Cai, G.X. Liang, D.P. Zhang, F. Ye, Y. Z. Li, Q.Y. Lin, Enhanced thermoelectric properties of mixed zinc antimonide thin films via phase optimization, *Appl. Surf. Sci.* 292 (2014) 823–827.
- [40] Q.Y. Qiu, Y.T. Liu, K.Y. Xia, T. Fang, J.J. Yu, X.B. Zhao, T.J. Zhu, Grain boundary scattering of charge transport in n-Type (Hf,Zr)CoSb Half-Heusler thermoelectric materials, *Adv. Energy Mater.* 9 (11) (2019) 7.
- [41] L.H. Huang, R. He, S. Chen, H. Zhang, K. Dahal, H.Q. Zhou, H. Wang, Q.Y. Zhang, Z.F. Ren, A new n-type half-Heusler thermoelectric material NbCoSb, *Mater. Res. Bull.* 70 (2015) 773–778.
- [42] J. Wang, G. Yuan, J. Yu, X. Mo, Y. Jin, L. Huang, The Preparation of Half-Heusler Alloy TaCoSb and the influence of Sn doping on the thermoelectric properties, *J. Xihua Univ. (Nat. Sci. Ed.)* 37 (3) (2018) 68–72.
- [43] L.H. Huang, Y.M. Wang, J. Shuai, H. Zhang, S.Q. Zhang, Q.Y. Zhang, Z.F. Ren, Thermal conductivity reduction by isoelectronic elements V and Ta for partial substitution of Nb in half-Heusler $Nb(1-x)/2V(1-x)/2TaCoSb$, *RSC. Adv.* 5 (124) (2015) 102469–102476.
- [44] L.H. Huang, J.C. Wang, X.B. Mo, X.B. Lei, S.D. Ma, C. Wang, Q.Y. Zhang, Improving the thermoelectric properties of the Half-Heusler compound VCoSb by vanadium vacancy, *Materials* 12 (10) (2019) 8 (Basel).
- [45] N.S. Chauhan, D. Bhattacharjee, T. Maiti, Y.V. Kolen'ko, Y. Miyazaki, A. Bhattacharya, Low lattice thermal conductivity in a wider temperature range for biphasic-quaternary (Ti,V)CoSb Half-Heusler alloys, *ACS. Appl. Mater. Interfaces.* 14 (49) (2022) 54736–54747.
- [46] E. Rausch, M.V. Castegnaro, F. Bernardi, M.C.M. Alves, J. Morais, B. Balke, Short and long range order of Half-Heusler phases in (Ti,Zr,Hf)CoSb thermoelectric compounds, *Acta Mater.* 115 (2016) 308–313.
- [47] X. Yan, W.S. Liu, S. Chen, H. Wang, Q. Zhang, G. Chen, Z.F. Ren, Thermoelectric property study of nanostructured p-Type Half-Heuslers (Hf, Zr, Ti)CoSb_{0.8}Sn_{0.2}, *Adv. Energy Mater.* 3 (9) (2013) 1195–1200.
- [48] J. Al-Otaibi, G.P. Srivastava, Three-phonon scattering processes and thermal conductivity in IV-chalcogenides, *J. Phys. Condens. Matter* 27 (33) (2015) 13.
- [49] D.K. Ferry, Alloy scattering in ternary iii-v compounds, *Phys. Rev. B* 17 (2) (1978) 912–913.
- [50] C. Hu, K. Xia, C. Fu, X. Zhao, T. Zhu, Carrier grain boundary scattering in thermoelectric materials, *Energy Environ. Sci.* 15 (4) (2022) 1406–1422.
- [51] J.J. Kuo, S.D. Kang, K. Imasato, H. Tamaki, S. Ohno, T. Kanno, G.J. Snyder, Grain boundary dominated charge transport in Mg 3 Sb 2-based compounds, *Energy Environ. Sci.* 11 (2) (2018) 429–434.
- [52] R. He, D. Kraemer, J. Mao, L. Zeng, Q. Jie, Y. Lan, C. Li, J. Shuai, H.S. Kim, Y. Liu, Achieving high power factor and output power density in p-type half-Heuslers Nb_{1-x}Ti_xFeSb, *Proc. Nat. Acad. Sci.* 113 (48) (2016) 13576–13581.
- [53] E. Rausch, B. Balke, S. Ouardi, C. Felser, Enhanced thermoelectric performance in the p-type half-Heusler (Ti/Zr/Hf)CoSb_{0.8}Sn_{0.2} system via phase separation, *Phys. Chem. Chem. Phys.* 16 (46) (2014) 25258–25262.
- [54] T. Sekimoto, K. Kurosaki, H. Muta, S. Yamanaka, High-thermoelectric figure of merit realized in p-type half-Heusler compounds: $ZrCo_{1-x}Sb_x$, *Jpn. J. Appl. Phys. Part 2 Lett. Express Lett.* 46 (25–28) (2007) L673–L675.
- [55] M. Zhou, L.D. Chen, W.Q. Zhang, C.D. Feng, Disorder scattering effect on the high-temperature lattice thermal conductivity of TiCoSb-based half-Heusler compounds, *J. Appl. Phys.* 98 (1) (2005) 5.
- [56] S. Liu, Y. Hu, S.N. Dai, Z.R. Dong, G.Q. Wu, J. Yang, J. Luo, Synergistically optimizing electrical and thermal transport properties of ZrCoSb through Ru doping, *ACS. Appl. Energy Mater.* 4 (12) (2021) 13997–14003.
- [57] R. He, T.S. Zhu, P.J. Ying, J. Chen, L. Giebeler, U. Kuhn, J.C. Grossman, Y.M. Wang, K. Nielsch, High-pressure-sintering-induced microstructural engineering for an ultimate phonon scattering of thermoelectric half-Heusler compounds, *Small.* 17 (33) (2021) 9.
- [58] S. Li, F.X. Bai, R.F. Wang, C. Chen, X.F. Li, F. Cao, B. Yu, J.H. Sui, X.J. Liu, Z.F. Ren, Q. Zhang, Titanium doping to enhance thermoelectric performance of 19-electron VCoSb half-Heusler compounds with vanadium vacancies, *Ann. Phys.* 532 (11) (2020) 7.
- [59] Y.T. Liu, C.G. Fu, K.Y. Xia, J.J. Yu, X.B. Zhao, H.G. Pan, C. Felser, T.J. Zhu, Lanthanide contraction as a design factor for high-performance half-Heusler thermoelectric materials, *Adv. Mater.* 30 (32) (2018) 7.
- [60] S.K. Bux, M.T. Yeung, E.S. Toberer, G.J. Snyder, R.B. Kaner, J.P. Fleurial, Mechanochemical synthesis and thermoelectric properties of high quality magnesium silicide, *J. Mater. Chem.* 21 (33) (2011) 12259–12266.
- [61] H.H. Xie, H. Wang, Y.Z. Pei, C.G. Fu, X.H. Liu, G.J. Snyder, X.B. Zhao, T.J. Zhu, Beneficial contribution of alloy disorder to electron and phonon transport in half-Heusler thermoelectric materials, *Adv. Funct. Mater.* 23 (41) (2013) 5123–5130.